

Electrochemical performance of copper phosphosulfide (Cu_3PS_4) towards magnesium ion storage

Debashis Tripathy , S. Sampath

PII: S0013-4686(23)00502-9
DOI: <https://doi.org/10.1016/j.electacta.2023.142324>
Reference: EA 142324



To appear in: *Electrochimica Acta*

Received date: 2 January 2023
Revised date: 14 March 2023
Accepted date: 29 March 2023

Please cite this article as: Debashis Tripathy , S. Sampath , Electrochemical performance of copper phosphosulfide (Cu_3PS_4) towards magnesium ion storage, *Electrochimica Acta* (2023), doi: <https://doi.org/10.1016/j.electacta.2023.142324>

This is a PDF file of an article that has undergone enhancements after acceptance, such as the addition of a cover page and metadata, and formatting for readability, but it is not yet the definitive version of record. This version will undergo additional copyediting, typesetting and review before it is published in its final form, but we are providing this version to give early visibility of the article. Please note that, during the production process, errors may be discovered which could affect the content, and all legal disclaimers that apply to the journal pertain.

Highlights

- Cu_3PS_4 and Cu_3PS_4 -SWCNT composite have been synthesized and characterized.
- Rechargeable Mg battery with high capacity and cycling stability are achieved.
- Rate performance up to 2 A g^{-1} is observed.
- *Ex situ* Raman and XPS studies reveal conversion reaction as the mechanism of storage.

Electrochemical performance of copper phosphosulfide (Cu_3PS_4) towards magnesium ion storage

Debashis Tripathy and S. Sampath*
Department of Inorganic and Physical Chemistry
Indian Institute of Science, Bangalore-560012, India
Email: sampath@iisc.ac.in

Abstract

Rechargeable magnesium batteries are good alternates for large scale energy storage applications and development of electrolytes as well as electrode materials are being pursued. In the present study, a cost-effective electrode material made of naturally abundant elements, Cu_3PS_4 is proposed for rechargeable magnesium battery. The electrochemical performance of Cu_3PS_4 is evaluated in different potential ranges. Further enhancement in the performance is achieved by using a carbon nanotube composite. The optimized electrode can deliver high capacity of 130 mAh g^{-1} at 50 mA g^{-1} current density and high cycling stability of 500 cycles with 80% capacity retention at 1000 mA g^{-1} current density at room temperature. The possible mechanism for Mg^{2+} storage is probed by *ex-situ* X-ray diffraction (XRD), Raman spectroscopy and X-ray photoelectron spectroscopy (XPS).

Key words: Rechargeable magnesium battery, Magnesium storage, Cu_3PS_4 , MWCNT composite, high capacity

1. Introduction

Rechargeable metal ion batteries are widely used in electronic gadgets and high-end applications such as electric vehicles and grid storage. In this direction, magnesium based rechargeable batteries have been explored as good alternates to the present generation batteries. Magnesium that possesses a high volumetric capacity (3833 mAh cm^{-3}) and almost dendrite-free and less reactive nature under ambient conditions strike out the safety concerns associated with certain other chemistries. Good electrochemical characteristics such as low equivalent weight and low reduction potential ($- 2.37 \text{ V vs. SHE}$) makes it a suitable electrode. In addition, high natural abundance (1.93% in earth's crust) and low equivalent weight are excellent positive attributes [1]. Despite the advantages, two major challenges hinder the development of rechargeable magnesium batteries, and they are (i) the absence of suitable electrolyte and (ii) electrode material. Most of the electrolytes form a passivating layer on the Mg surface and cannot be used for long term use. Although the size is smaller compared to Li^+ , high charge to size ratio of Mg^{2+} leads to a strong interaction with the host material and reduces the Mg^{2+} solid-state diffusion [2,3]. Hence, there is a need for the development of electrode materials. Though there have been several earlier studies on Mg based batteries [4,5], the one proposed by Aurbach et al. on Chevrel phases, Mo_6S_8 [6] has rekindled the interest in this area. Subsequently, several materials have been investigated as hosts for rechargeable magnesium batteries that include, Chevrel phase $\text{Mo}_6\text{S}_{8-x}\text{Se}_x$ ($x < 4$) [7], MgFePO_4F [8], transition metal oxides [3,9–11], transition metal chalcogenides MX_2 ($\text{M} = \text{Ti, V, Mo, Zr, W, Cu, X} = \text{S, Se}$) [9,12–16] and polyanionic compounds $\text{Mg}_x\text{M}_y\text{SiO}_4$ ($\text{M} = \text{Mn, Fe, Co, } x + y = 2$) [17–19].

Transition metal sulphides show considerable Mg mobility as compared to transition metal oxides due to the lower polarizing power of sulphide than that of the oxide [16]. Complete utilization of oxidation states in conversion mechanism helps achieve high capacity

unlike intercalation process [20]. CuS as a conversion electrode has been known for its high magnesium storage capacity in different electrolytes under ambient conditions and both half-cell and full-cell configurations have been reported at different temperatures [16,21,22]. Nanosized CuS with an improved interface in magnesium bis(hexamethyldi-silazide) [Mg(HMDS)₂]-aluminum chloride (AlCl₃) in dimethoxyethane (DME) electrolyte has been shown to deliver high capacities [21]. CuS has also been studied as a flexible electrode along with multiwalled carbon nanotubes (MWCNT) and is reported to deliver a high capacity in a hybrid electrolyte [23]. Cu₃P is also known to be a good electrode material for Li-ion [24,25] and Al-ion [26] batteries. In recent literature, a combination of phosphide and chalcogenide, metal phosphochalcogenides (MPX₃, M: Fe, Co, Ni, Sn and X: S, Se) have emerged as promising electrode materials for Li, Na and Mg-ion batteries [27–30]. In this direction, Cu₃PS₄ has been reported to be a good electrode material for Li and Na-ion batteries [31,32]. Hence, it is expected that the inclusion of phosphorus and sulphur along with copper may have combined advantages for magnesium batteries as well.

In the present study, use of Cu₃PS₄ has been shown to yield high capacities along with high cycling stability under ambient conditions. An improvement is observed when a multiwalled carbon nanotube (MWCNT) composite with the phosphochalcogenide is used. The composite electrode shows a stable capacity of 130 mAh g⁻¹ at 50 mA g⁻¹ current density in the potential window 0.01-2.2 V vs. Mg²⁺/Mg. Further, at a high current density of 500 mA g⁻¹, stable cycling behaviour is observed. The underlying mechanism behind magnesium storage is understood using *ex-situ* Raman spectroscopy, X-ray diffraction and X-ray photoelectron spectroscopy techniques.

2. Experimental

2.1. Material synthesis

Cu_3PS_4 was synthesized by chemical vapor transport (CVT) method as explained in our earlier paper [31]. MWCNT was treated with nitric acid and washed thoroughly with deionized water to remove impurities if any. Pre-treated MWCNT was used for the composite preparation. MWCNT (10 mg) was dispersed in ethanol (5 mL) to which Cu_3PS_4 (40 mg) was added and sonicated for 2 h. The composite was collected by centrifugation after washing with ethanol a few times and dried at 80 °C for 4 h. The as-synthesized material and composite were used for characterization.

2.2. Characterization

The X-ray diffraction (XRD) patterns of pristine and carbon nanotube composite materials were collected using Philips (PAN Analytical) X-ray BV diffractometer (X-ray source- $\text{Cu K}\alpha$ (1.5418 Å)). Raman spectra and mapping measurements were conducted using a Raman spectrometer (LabRAM HR Evolution, Horiba Jobin Yvon, France) with the help of 514 nm excitation laser. The X-ray photoelectron spectrometer (Thermo K-alpha, X-ray source- $\text{Al K}\alpha$ (1486.6 eV)) was used for all the X-ray photoelectron spectroscopic (XPS) measurements. A field emission scanning electron microscope (FE-SEM) (Carl Zeiss ultra 55) was used for imaging and elemental mappings of the materials and electrodes. After the electrochemical studies, the cells were disassembled inside the glovebox and thoroughly washed with THF to get rid of residual electrolyte. These electrodes then vacuum dried and subsequently transferred to the spectrometer from the glovebox using a vacuum transfer module for XPS analyses.

2.3. Electrochemical measurements

All the electrochemical studies were conducted using CR 2032 type coin cells assembled inside an argon-filled glove box (Jacomex) with moisture and oxygen content below 0.5 ppm. The slurry (active material: carbon: polyvinylidene fluoride= 7:2:1 wt% with few drops of N-methyl pyrrolidone) was coated on molybdenum (Mo) substrate and vacuum dried at 80 °C

for 12h. in an oven to use as electrodes. An electrolyte made of magnesium bis(hexamethyl-disilazane) ($\text{Mg}(\text{HMDS})_2$) and magnesium chloride (MgCl_2) (1:4 mol ratio) in tetrahydrofuran (THF) and N-methyl-N-propyl-piperidinium bis(trifluoromethane sulfonyl)imide ($\text{PP}_{13}\text{TFSI}$) (2:1 v/v) or $\text{MMTP}_{13}\text{TFSI}$ was used as the electrolyte. Magnesium foils (Goodfellow, UK) were used as anodes. These foils were cleaned with fine grade emery paper and wiped with tissue paper just before assembling the cells. All the electrochemical measurements were carried out using Biologic instrument (VSP 300). Cyclic voltammetry and galvanostatic charge-discharge measurements were performed in different potential ranges between 0.01 and 2.2 V vs. Mg^{2+}/Mg . The specific capacities were calculated based on the weight of Cu_3PS_4 or $\text{Cu}_3\text{PS}_4\text{-MWCNT}$ composite in the electrodes. Galvanostatic intermittent titration technique (GITT) was performed with a 900 s discharge/ charge step followed by 1200 s rest period after each step in the same potential window using Biologic instrument (VSP 300). Impedance measurements were performed in 100 kHz-10 mHz frequency range with a sinusoidal pulse of 10 mV amplitude.

3. Result and Discussion

The as-synthesized Cu_3PS_4 is characterized by X-ray diffraction (XRD), Raman spectroscopy and X-ray photoelectron spectroscopy (XPS) techniques. As observed earlier, Cu_3PS_4 crystallizes in orthorhombic structure (space group, $\text{Pmn}2_1$; $a = 7.2781 \text{ \AA}$, $b = 6.3300 \text{ \AA}$ and $c = 6.0751 \text{ \AA}$) [31] and the unit cell structure is shown in Fig. S1. Fig. 1a compares the XRD patterns of Cu_3PS_4 and $\text{Cu}_3\text{PS}_4\text{-MWCNT}$ composite along with the standard XRD pattern (JCPDS # 01-073-1996). The composite contains all the peaks of Cu_3PS_4 at the same positions along with an additional peak at $2\theta = 24^\circ$ (highlighted in pink) that corresponds to MWCNT. Raman microscopy reveals uniform distribution of elements, and the composition is uniform throughout the Cu_3PS_4 crystal as shown in Fig. 1b and the bands are assigned to different vibrational modes. The images obtained from Raman mapping for each individual

modes match well with the optical image of the material [33,34]. In the Raman spectrum, two extra bands are observed for the composite at 1350 cm^{-1} and 1580 cm^{-1} along with the bands that belong to Cu_3PS_4 as shown in Fig. 1c. These two bands are attributed to the D band and G band of MWCNT corresponding to the disordered carbon and graphitic carbon, respectively. Fig. 1d-f compare the high resolution XPS data of pristine Cu_3PS_4 and its MWCNT composite. The binding energies values of the composite are slightly shifted to lower side as compared to pristine Cu_3PS_4 indicating an interaction between MWCNT and Cu_3PS_4 . The morphology of

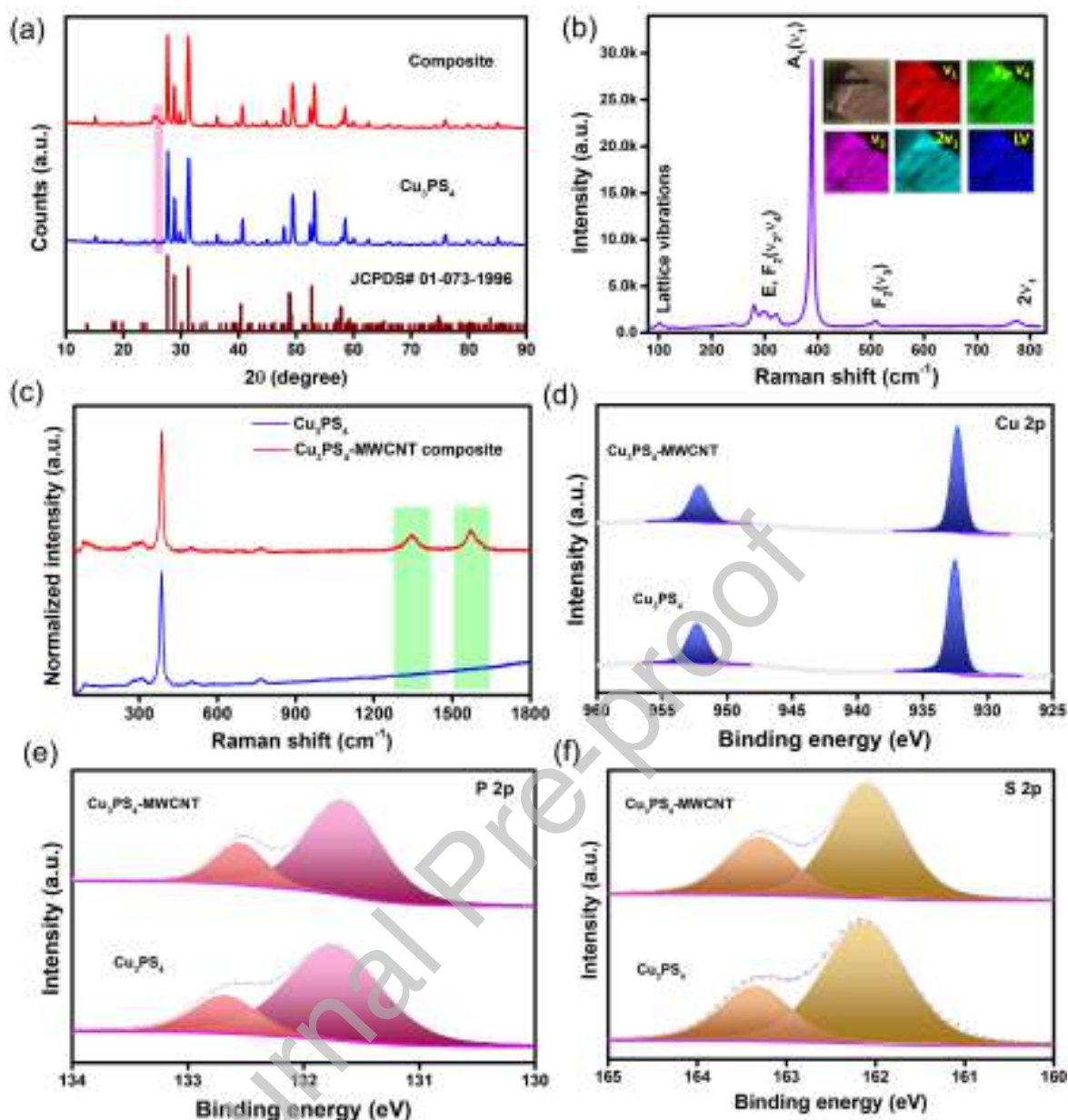


Fig. 1. Characterization of Cu_3PS_4 and Cu_3PS_4 -MWCNT composite. (a) XRD patterns along with the standard pattern, (b) Raman mapping of Cu_3PS_4 (c) Raman spectra for Cu_3PS_4 and the composite, X-ray photoelectron spectra of (d) Cu 2p, (e) P 2p and (f) S 2p regions of pristine Cu_3PS_4 and its MWCNT composite.

Cu_3PS_4 and Cu_3PS_4 -MWCNT composite are investigated by scanning electron microscopy. The pristine phosphosulphide shows a layer-type morphology as observed in Fig. 2a. The morphology is retained in the composite (Fig. 2b) wherein Cu_3PS_4 is entangled by the MWCNT (inset of Fig. 2b). A homogeneous distribution of Cu, P and S is observed

throughout Cu_3PS_4 and the composite indicating uniformity of the composition (Fig. 2c and d).

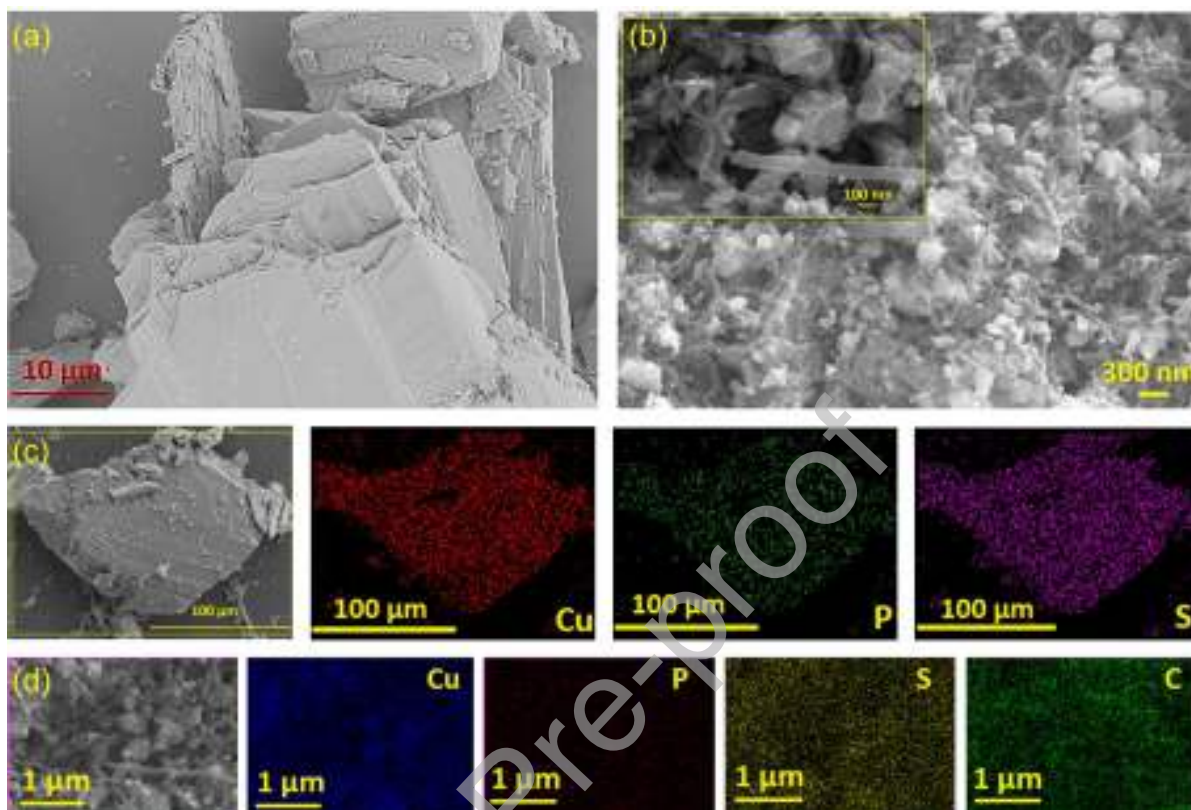


Fig. 2. SEM images of (a) Cu_3PS_4 and (b) Cu_3PS_4 -MWCNT composite, elemental mapping of (c) Cu_3PS_4 and (d) MWCNT composite respectively.

The electrochemical Mg-ion storage performance of Cu_3PS_4 is evaluated in the coin cell configuration using $\text{MMTP}_{13}\text{TFSI}$ electrolyte and Mg metal anode in different potential windows. Fig. 3a compares the discharge capacities of the Cu_3PS_4 electrodes in two different potential ranges at a discharge rate of 50 mA g^{-1} . A stable capacity of 50 mAh g^{-1} is observed in the potential window 0.2-2.1 V while 108 mAh g^{-1} capacity is obtained in the potential window 0.01-2.2 V. In the latter potential window, the stable capacity value is obtained after 30 cycles whereas 100 cycles are required in the former potential window (Fig. S2). However, a gradual increase in the capacity is observed in the initial stages that suggests an activation process. In the case of 0.01-2.2 V window, it takes a smaller number of cycles to obtain a stable capacity and the activation process occurs fast. The reason behind the faster

activation process will be discussed later. Fig. 3b shows the galvanostatic charge-discharge cycles in the potential window 0.01-2.2 V at 50 mA g⁻¹ current. Fairly well- distinguished plateaus are observed with an increasing trend in capacity that stabilizes after certain number of cycles. Further, a gradual decrease in polarization with cycling is also observed from Fig. 3b. It indicates that activation

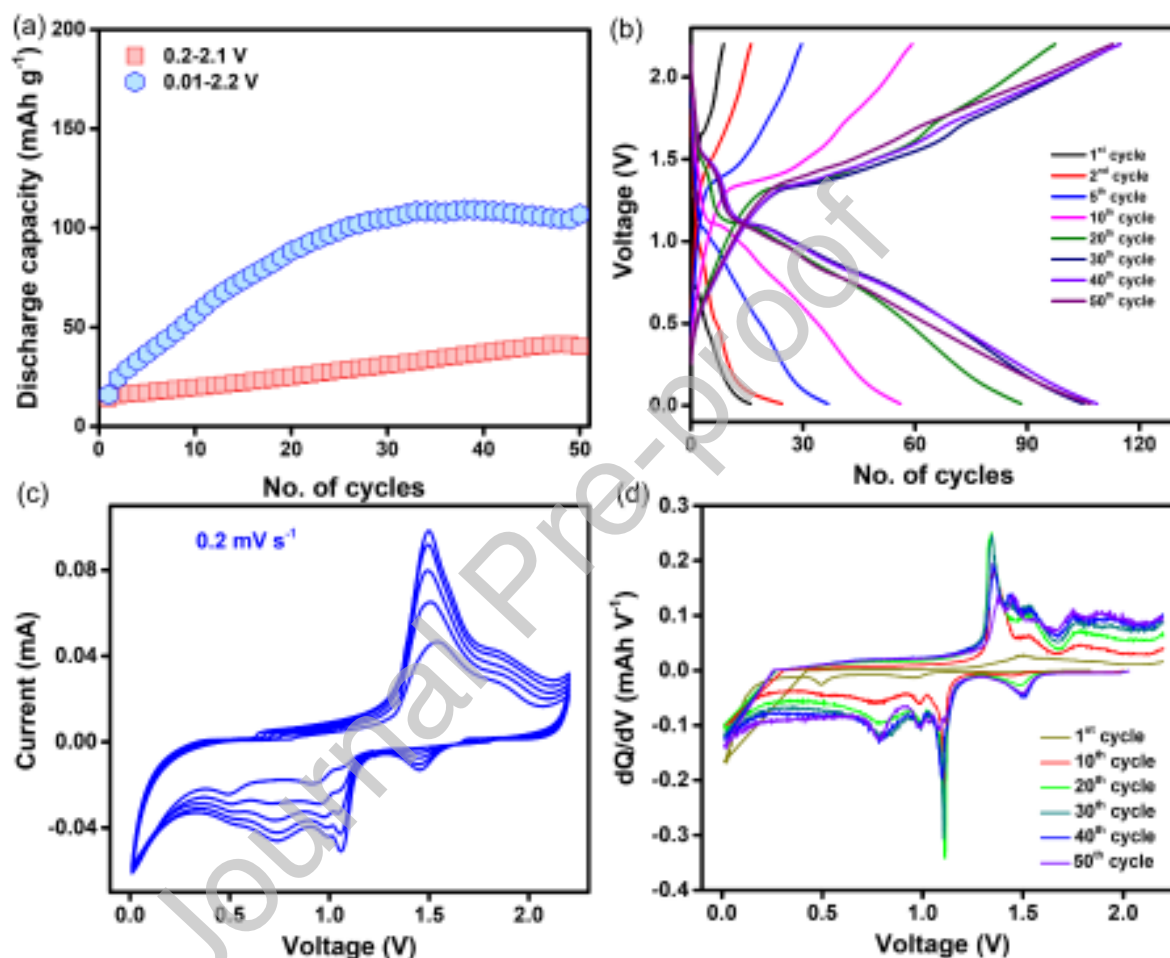


Fig. 3. (a) Discharge capacity as a function of cycling in different potential windows at a rate of 50 mA g⁻¹, (b) galvanostatic charge-discharge cycles at 50 mA g⁻¹, (c) cyclic voltammograms at 0.2 mV s⁻¹ and (d) dQ/dV plots corresponding to the galvanostatic charge-discharge cycles in the potential window 0.01-2.2 V for Cu₃PS₄ electrode.

process for the electrode is faster in this potential window as compared to the earlier one (0.2-2.1 V). For the first cycle, the discharge and charge capacities are 16 and 9 mAh g⁻¹,

respectively. A gradual increase in the capacity is observed up to 30 cycles after which the capacity is stabilizes at 108 mAh g^{-1} as shown in Fig. 3a.

For the initial cycles, the coulombic efficiency observed is higher than 100% which then stabilizes at $\sim 94\%$. The coulombic efficiency fluctuates from 100% at this current density may be due to self-discharge of the electrode. The cyclic voltammograms obtained at a scan rate of 0.2 mV s^{-1} is shown in Fig. 3c. The plateaus observed in charge-discharge behaviour correspond to the peaks in cyclic voltammograms. A peak around 1.45 V corresponds to the insertion of Mg^{2+} ions in Cu_3PS_4 . The two peaks located close to 1 V (1.06 and 0.98 V) may be due to the stepwise conversion reaction of Mg^{2+} with Cu_3PS_4 . A broad peak around 0.7 V may be due to a change in the oxidation state of Cu and formation of Mg-S species. Only two oxidation peaks are observed, a sharp one at 1.5 V and a very broad peak at 1.85 V that correspond to reverse reactions. The dQ/dV plots (Fig. 3d) obtained from the galvanostatic charge-discharge cycles show peaks similar to that of the cyclic voltammograms. It is observed that the peak currents increase initially, then remain constant and thereafter decrease to a small extent. This is likely to be due to full conversion of the electrode material after certain number of cycles. The capacity decreases after certain number of cycles since the products of conversion reactions may be not very active for Mg.

The performance of the electrodes can be improved by forming composites with conducting carbonaceous materials. MWCNT finds its use in various energy storage applications owing to high active surface area, good chemical stability, and electrical conductivity. Further, it provides conducting pathways for the migration of ions and electrons and the increased interface area leads to faster ion diffusion. CuS-CNT composite and $\alpha\text{-MoS}_3$ -CNT nanowire electrodes are reported to deliver better performance than that of the pristine

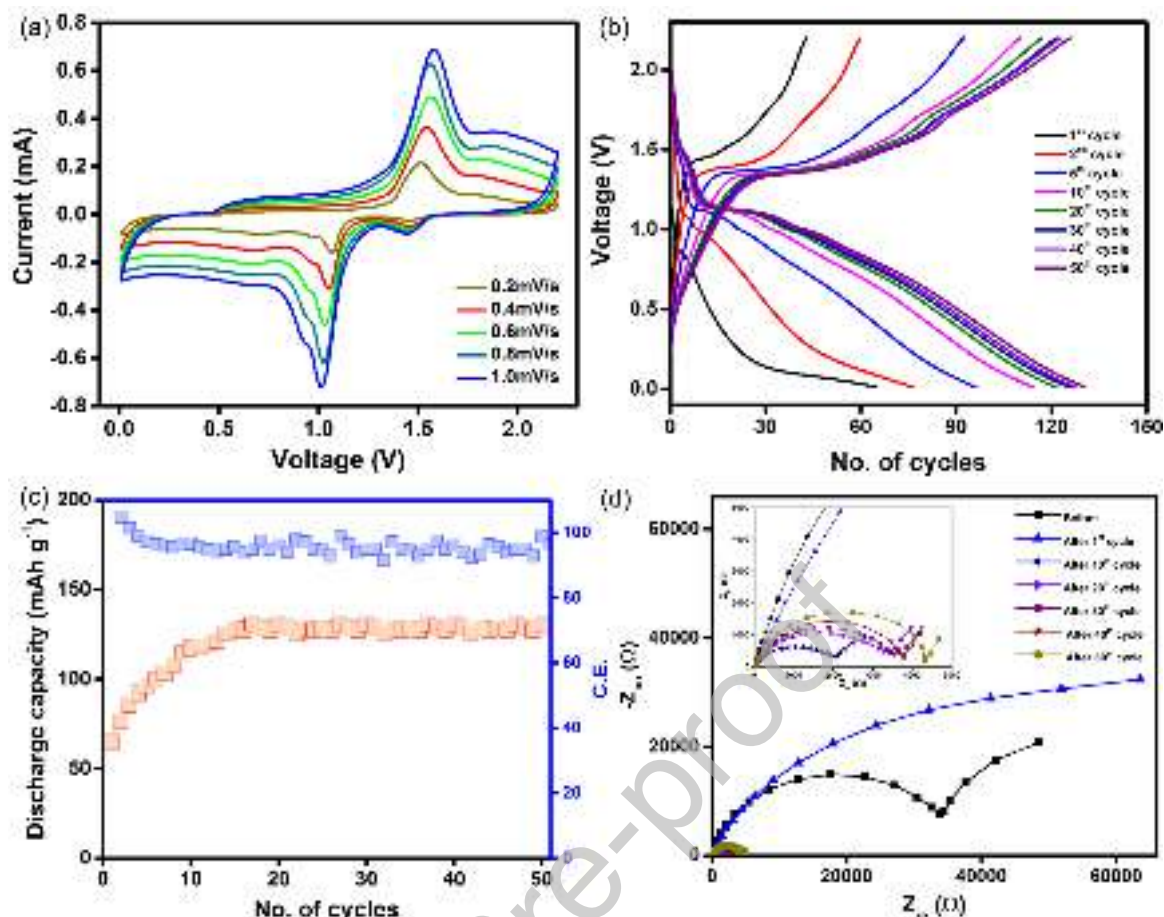


Figure. 4 (a) Cyclic voltammograms at different scan rates (from 0.2-1.0 mV s^{-1}); (b) galvanostatic charge-discharge cycles and (c) cycling performance and coulombic efficiency at a rate of 50 mA g^{-1} and (d) Nyquist plots after various charge-discharge cycles for the Cu_3PS_4 -MWCNT electrode.

electrodes [17,23,35,36]. Further, the use of MWCNT also helps in stabilizing the intermediate products of Mg-S batteries [37]. The cyclic voltammograms for the initial cycles at a scan rate of 0.2 mV s^{-1} are shown in Fig. S3. The voltammograms resemble that of Cu_3PS_4 but are more stable with increased peak current for the composite. The voltammograms at different scan rates from 0.2 to 1.0 mV s^{-1} are recorded in the same potential window and are shown in Fig. 4a. Similar reversible cathodic and anodic peaks are observed at all scan rates indicating excellent rate performance of the composite. These peaks

show a good linear dependence of peak current (i) vs. scan rate (v) as shown in Fig. S4a which indicates a surface controlled

capacitive process during the charge and discharge process.

The 'b' values are obtained from the slope of logarithmic plots ($\log i$ vs. $\log v$) using the power law equation (equation 1),

$$i_p = a v^b \quad (1)$$

where i_p is the peak current, v is the scan rate and a , b are constants. The obtained 'b' values (Fig. S4b) are found to be close to 1 indicating a surface controlled capacitive process. The galvanostatic charge-discharge curves for the composite at 50 mA g^{-1} are depicted in Fig. 4b. Very high polarization is observed for the initial cycles analogous to the earlier observations for the pristine compound which then gradually decreases indicating the formation of a stable interface at the electrode along with a continuous activation process. The initial discharge and charge capacities are 65 mAh g^{-1} and 40 mAh g^{-1} respectively and are larger than that of the pristine Cu_3PS_4 . Well defined plateaus are observed for the charge-discharge curves. However, the polarization in the case of composite is smaller than that of Cu_3PS_4 and it may be due to an improved conductivity of the composite and facile ion diffusion process. Fig. 4c shows the cycling stability at a rate of 50 mA g^{-1} . The capacity increases gradually and stabilizes at 130 mAh g^{-1} from 20th cycles onwards. The coulombic efficiency is more than 100% for the initial few cycles which then remains stable at 98% subsequently. The dQ/dV plots (Fig. S5) obtained from the galvanostatic charge-discharge curves shows peaks similar to that of the voltammograms. Electrochemical impedance spectroscopy (EIS) has been carried out after charge-discharge cycles. Fig. 4d and Fig. S6 show the Nyquist plots for the composite and pristine Cu_3PS_4 after different charge-discharge cycles, respectively. The data comprise of a depressed semicircle and an inclined line at high to mid frequency and low frequency range, respectively. The charge transfer resistance for the as-prepared Cu_3PS_4

electrode is $100 \text{ k}\Omega \text{ cm}^2$ and reduces to $35 \text{ k}\Omega \text{ cm}^2$ for the composite. Further, the impedance values obtained for the composite is quite low as compared to pristine Cu_3PS_4 indicating faster charge transfer in the

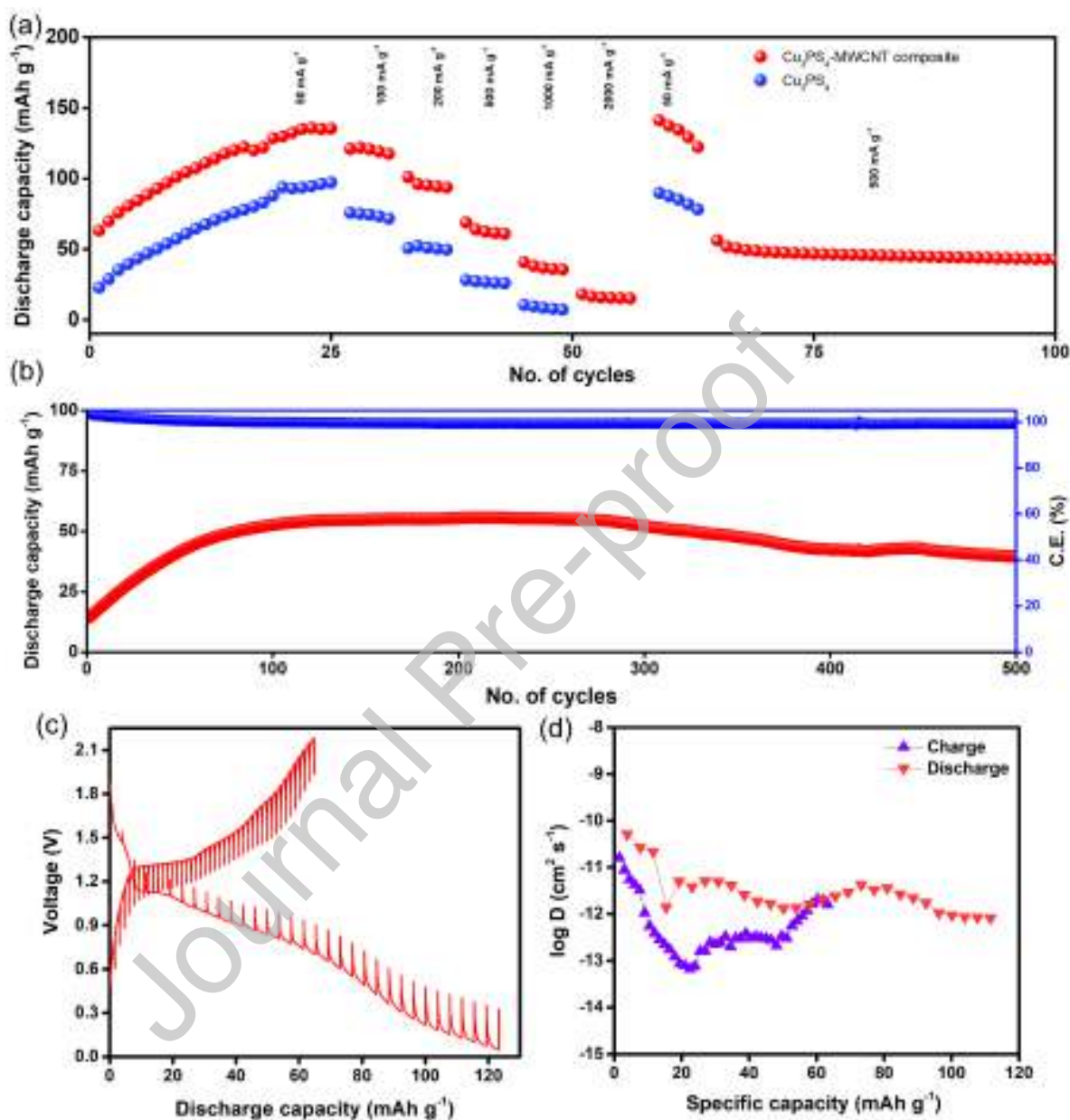


Figure. 5 (a) Comparison of rate performance for Cu_3PS_4 and the composite from 50 to 2000 mA g^{-1} current rate, (b) long term cycling stability at 1000 mA g^{-1} current density, (c) GITT profiles and (d) corresponding Mg^{2+} diffusion coefficients for the composite electrode.

case of composite that in turn improves the performance. A high impedance value after the first cycle may be due to a change in the Mg anode surface and in the electrode material due

to Mg^{2+} insertion/ extraction [38]. However, a gradual decrease in the charge transfer resistance with cycling confirms the activation process and stabilization of the product formed during cycling. The values remain almost constant up to 40th cycle after which a small increase in the charge transfer value is observed. It may be due to passivation/ blocking of the Mg metal anode surface with prolonged cycling.

Fig. 5a compares the rate performance of Cu_3PS_4 and the composite at different current densities from 50 to 2000 mA g^{-1} . For the initial cycles, the capacity increases and hence, the performance is compared after the capacity is stabilized. At all current densities, the capacity obtained for the composite is larger than that of Cu_3PS_4 . For Cu_3PS_4 , the capacity obtained is very low at a high discharge rate of 1000 mA g^{-1} while it is 30 mAh g^{-1} for the composite. The cycling performance at high rate for the composite indicates the synergetic effect of the composite. Clear plateaus are observed at all current densities indicating a reversible system. The long-term cycling stability for both the electrodes are compared at 500 mA g^{-1} current density (Fig. S7). For Cu_3PS_4 , the capacity decreases gradually after a maximum value and at the end of 300 cycles, the obtained capacity 13 mAh g^{-1} which is 30% of the maximum capacity. A capacity of 55 mAh g^{-1} is observed for the composite at the end of 300 cycles and is 80% capacity retention of the maximum value with a coulombic efficiency of 100%. Even at a high discharge current of 1000 mA g^{-1} , the composite delivers 500 cycles (Fig. 5b) with a capacity retention of 90% and 100% coulombic efficiency.

The diffusion coefficients for Mg^{2+} diffusion is calculated from the galvanostatic intermittent titration technique (GITT) measurements assuming that the transport of Mg^{2+} is controlled by Fick's second law of diffusion. Before this experiment, the cell was cycled at 50 mA g^{-1} for 5 cycles. Fig. 5c shows the GITT curves obtained at constant current of 10 mA

g^{-1} in the potential range of 0.01-2.2 V for 900 s followed by a rest time of 1200 s to attain a steady-state potential. The diffusion coefficient is calculated using the equation 2 [39]-

$$D_{\text{Mg}^{2+}} = \frac{4}{\pi\tau} \left(\frac{m_B V_M}{M_B S} \right)^2 \left(\frac{\Delta E_S}{\tau(dE_\tau / d\sqrt{\tau})} \right)^2 \quad (\tau \ll L^2/D) \quad (2)$$

where m_B , V_M and M_B are the mass, molar volume, and molecular mass of active material

Cu_3PS_4 , S is the geometric area of the electrode, M_B/V_M is the density, L is the average thickness of the electrode.

The above equation can be further simplified to equation 3 by considering linear behaviour of the cell voltage during the experiment and $\tau^{1/2}$.

$$D_{\text{Mg}^{2+}} = \frac{4}{\pi\tau} \left(\frac{m_B V_M}{M_B S} \right)^2 \left(\frac{\Delta E_S}{\Delta E_\tau} \right)^2 \quad (3)$$

where ΔE_S is change in steady state voltage after the applied current and relaxation process, ΔE_τ is the voltage change (after deducting iR drop) during the constant applied current. Diffusion coefficient is calculated by assuming constant molar volume (V_M). Fig. 5d shows the variation of diffusion coefficients at different stages of charge-discharge processes. These coefficients are in the range of 10^{-11} - $10^{-14} \text{ cm}^2 \text{ s}^{-1}$ which are of same order as that of other inorganic electrodes like Mo_6S_8 , CuS , FePS_3 and $\alpha\text{-MoS}_3$ [6,23,30,36].

The Mg^{2+} ion storage mechanism and the composition after cycling are investigated by *ex situ* XRD, Raman spectroscopy, XPS and SEM techniques. Fig. S8 shows the XRD patterns of the composite after various charge-discharge cycles. The peaks of Cu_3PS_4 gradually weaken and broaden as the cycling progresses. However, the presence of peaks for Cu_3PS_4 after cycling indicates incomplete structural conversion. The broadening of the peaks is a signature of conversion reaction. A continuous broadening of the peaks is observed that may be due to the amorphization Cu_3PS_4 as evident from the XRD patterns and is reported for FePS_3 electrode [30]. Further, the particle size changes from large size to small (Fig. S9)

pointing to amorphization. Hence, the initial increase in the capacity for few cycles may be attributed to continuous amorphization that facilitates the magnesium insertion/ deinsertion process. The elemental mapping of the electrodes after discharge and charge shows uniform distribution of the elements Cu, P, S and Mg (Fig. S10). In addition, after the charging process, Mg is still observed in the electrode indicating that there is incomplete demagnesiumation suggesting an

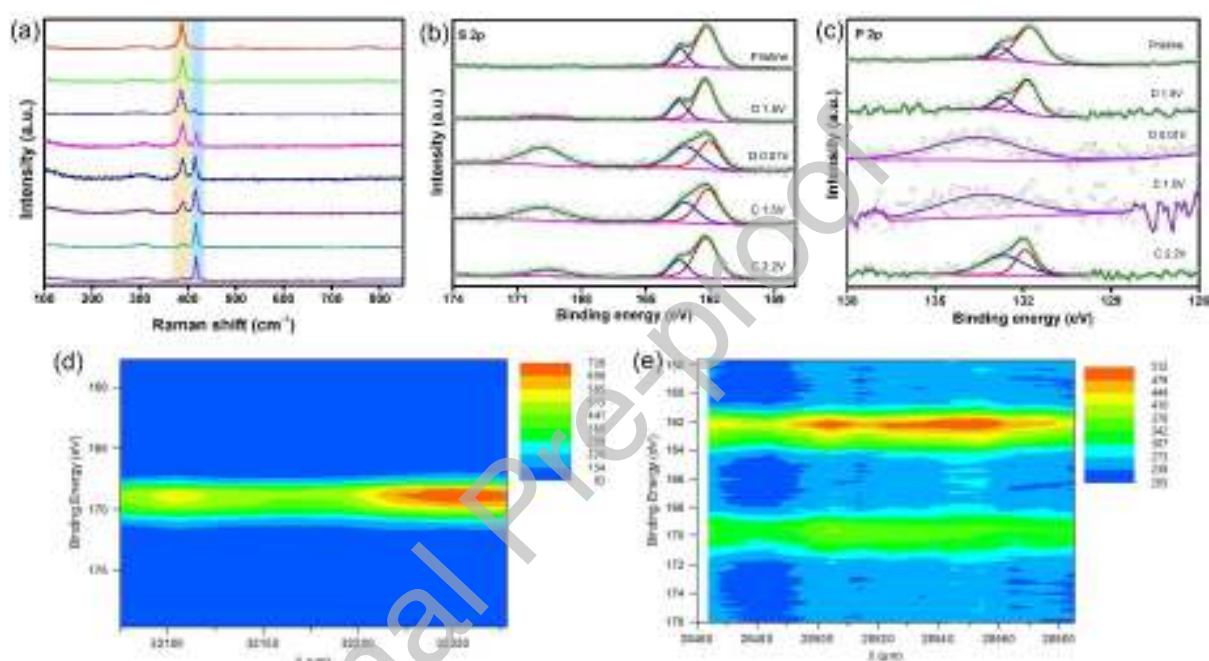


Figure. 6 (a) Raman spectra at different points on the electrode surface after a few charge-discharge cycles and high resolution XPS data of the electrodes at different stages (b) S 2p, (c) P 2p and (d) Mg 2p regions, XPS mapping of S 2p region for (d) the separator and (e) electrode surface after long-term cycling at 50 mA g⁻¹ rate.

irreversible reaction. The Raman spectra for the electrode at different points after charge-discharge cycles are shown in Fig. 6a. At different points, the spectra are different indicating non-uniform insertion/ de-insertion or reaction of magnesium with the electrode material. Similar uneven reaction / conversion is known in the literature for Li-ion batteries in the case of oxide-based cathodes such as LiCoO₂. Along with the main band of Cu₃PS₄ at 390 cm⁻¹ (highlighted in yellow) another band (highlighted in sky blue) is observed at 416 cm⁻¹. The

intensity of 416 cm^{-1} band gradually increases with a concomitant reduction intensity for the band at 390 cm^{-1} and at a certain point the band at 390 cm^{-1} disappears. At some places on the electrode surface, the conversion is partial while at others, a complete conversion is noted. The new band at 416 cm^{-1} may be due to the composition, $\text{Cu}_{3-2x}\text{Mg}_x\text{PS}_4$ or Mg^{2+} coordinated with phosphosulfide unit. It is difficult to predict exact the mechanism since there are multiple possibilities and the same is true for the exact composition. Similarly, at different points, Raman spectra (Fig. S11) of the electrode cycled in the range of $0.2 - 2.1\text{ V}$ show non-uniform reaction, but the intensity of the band at 416 cm^{-1} is less than that of the P-S stretching band. It indicates a slow interaction of Mg with Cu_3PS_4 in $0.2 - 2.1\text{ V}$ range. Hence, the activation process takes a longer time in this potential range as observed in Fig. 3a.

Further, X-ray photoelectron spectra are recorded at different stages of charge-discharge process. The redox chemistry of Cu_3PS_4 is complex as the elements are present in various oxidation states that can be reduced or oxidised during electrochemical studies. Similarly, the possibility of P_xS_y formation cannot be ignored. Fig. 6b shows the S 2p spectra of the electrode at different stages of charge-discharge process. An additional peak is observed around 169.5 eV which is due to TFSI anion along with the original S 2p_{3/2} and 2p_{1/2} peaks when the cell is discharged to 1.5 V , and it intensifies after full discharge. This peak intensity is reduced after charging the cell to 2.2 V . The presence of this peak indicates the adsorption TFSI anion on the electrode surface. The S 2p_{3/2} and 2p_{1/2} peaks are shifted to a slightly lower value for the fully discharged electrode (0.01 V) and remains same in the charged state till 1.5 V . For the fully charged electrode, the binding energy shifts to its original position. However, a noticeable change is observed in the case of P 2p spectra (Fig. 6c). The 2p_{3/2} and 2p_{1/2} peaks vanish after complete discharge to 0.01 V and a new peak appears at 133.45 eV . It is likely to be due to the formation of P_xS_y species during discharge

process and change in valence of P as observed in the case of FePS_3 [30,40]. The new peak remains intact after charging to 1.5 V and reduces when the electrode is completely charged. The $2p_{3/2}$ and $2p_{1/2}$ peaks reappear for the completely charged electrode but with a slight shift in the binding energy. The observed changes in the binding energies of P and S are likely to be due to a charge redistribution as result of Mg^{2+} ion intercalation and partial change in the oxidation state of Cu. This is similar to the observations made during Li intercalation in nickel phosphosulfide [41]. The structure of Cu_3PS_4 reveals no direct bond between Cu and P while Cu forms a tetrahedron with four S units and P forms a polyhedral with four S units. Hence, the disappearance of the original P 2p peaks after discharge to 0.01 V suggests the cleavage of P-S bond and re-appearance of the peaks for the completely charged electrode suggests the formation of the P-S bond again. However, shift of S 2p peaks to lower binding energy suggests formation of Mg-S complex.

To check whether there is polysulfide shuttling, Raman spectra of the separator and XPS mapping of S 2p region of both the separators and electrode are recorded after long-term cycling. No additional peak due to polysulfide is observed in the Raman spectra (Fig. S11). A new band due to Mg interaction with Cu_3PS_4 at 416 cm^{-1} is observed which suggests that the Mg interaction happens at the surface, and is probably mediated through the electrolyte onto the separator. XPS mapping of the separator (Fig. 6d) shows the peaks related to only TFSI anion and no other peak is observed indicating absence of any polysulfide. Similarly, for the electrode after long-term cycling (Fig. 6e), no sign of polysulfides (expected at lower binding energy side) is observed. However, a new peak is observed very close to 162 eV which could possibly suggest the formation of MgS_x . Further, to observe any change in the oxidation state of Cu, XPS mapping of Cu LMM region (Fig. S12) of the same electrode is performed which indicate the presence of Cu in +1 oxidation state. Further, no peak is observed around $470\text{--}474\text{ cm}^{-1}$ in the Raman spectra (Fig. 6a). These observations rule out the presence of CuS/

Cu₂S during cycling. As evident from the Mg 2p data (Fig. S13), the peak intensity is large for the discharged state while it reduces for the fully charged electrode which agrees well with SEM elemental mapping data. Hence, the storage process involves initial Mg interaction with Cu₃PS₄ forming magnesiated species (Cu_{3-2x}Mg_xPS₄) which then convert to Mg_xPS_y and MgS_x species. However, further experimental, and computational investigations are necessary to understand the exact mechanism.

4. Summary

In summary, Cu₃PS₄ and its MWCNT composite are synthesized and the Mg²⁺ storage

performance is compared. The composite is found to deliver better performance as a good conducting path is created between the material and MWCNT. Good rate performance with ~75 and 60 mAh g⁻¹ capacities at 500 and 1000 mA g⁻¹ current rates are observed. The long-term cycling stability is demonstrated by cycling the electrode at 1000 mA g⁻¹ that shows 80% capacity retention at the end of 500 cycles. The Mg²⁺ storage mechanism as probed by various *ex-situ* techniques shows insertion/ deinsertion and conversion reaction are responsible for the observed performance.

Declaration of competing interest

The authors do not have any competing interests.

Acknowledgement

DT thanks IISc. for a research fellowship. SS thanks IRHPA-SERB for funds through a project on the development of batteries.

References

- [1] J. Muldoon, C.B. Bucur, T. Gregory, Quest for Nonaqueous Multivalent Secondary Batteries: Magnesium and Beyond, Chem. Rev. 114 (2014) 11683–11720.

<https://doi.org/10.1021/cr500049y>.

- [2] F. Liu, T. Wang, X. Liu, L. Fan, Challenges and Recent Progress on Key Materials for Rechargeable Magnesium Batteries, *Adv. Energy Mater.* 11 (2021) 2000787. <https://doi.org/10.1002/aenm.202000787>.
- [3] J. Song, E. Sahadeo, M. Noked, S.B. Lee, Mapping the Challenges of Magnesium Battery, *J. Phys. Chem. Lett.* 7 (2016) 1736–1749. <https://doi.org/10.1021/acs.jpcllett.6b00384>.
- [4] P. Novák, J. Desilvestro, Electrochemical Insertion of Magnesium in Metal Oxides and Sulfides from Aprotic Electrolytes, *J. Electrochem. Soc.* 140 (1993) 140–144. <https://doi.org/10.1149/1.2056075>.
- [5] P. Novák, W. Scheifele, F. Joho, O. Haas, Electrochemical Insertion of Magnesium into Hydrated Vanadium Bronzes, *J. Electrochem. Soc.* 142 (1995) 2544–2550. <https://doi.org/10.1149/1.2050051>.
- [6] D. Aurbach, Z. Lu, A. Schechter, Y. Gofer, H. Gizbar, R. Turgeman, Y. Cohen, M. Moshkovich, E. Levi, Prototype systems for rechargeable magnesium batteries, *Nature* 407 (2000) 724–727. <https://doi.org/10.1038/35037553>.
- [7] D. Aurbach, G.S. Suresh, E. Levi, A. Mitelman, O. Mizrahi, O. Chusid, M. Brunelli, Progress in Rechargeable Magnesium Battery Technology, *Adv. Mater.* 19 (2007) 4260–4267. <https://doi.org/10.1002/adma.200701495>.
- [8] Z.-D. Huang, T. Masese, Y. Orikasa, T. Mori, T. Minato, C. Tassel, Y. Kobayashi, H. Kageyama, Y. Uchimoto, MgFePO_4F as a feasible cathode material for magnesium batteries, *J. Mater. Chem. A.* 2 (2014) 11578–11582. <https://doi.org/10.1039/C4TA01779J>.
- [9] T.D. Gregory, R.J. Hoffman, R.C. Winterton, Nonaqueous Electrochemistry of

- Magnesium: Applications to Energy Storage, *J. Electrochem. Soc.* 137 (1990) 775–780. <https://doi.org/10.1149/1.2086553>.
- [10] S. Rasul, S. Suzuki, S. Yamaguchi, M. Miyayama, High capacity positive electrodes for secondary Mg-ion batteries, *Electrochim. Acta.* 82 (2012) 243–249. <https://doi.org/10.1016/j.electacta.2012.03.095>.
- [11] S. Tepavcevic, Y. Liu, D. Zhou, B. Lai, J. Maser, X. Zuo, H. Chan, P. Král, C.S. Johnson, V. Stamenkovic, N.M. Markovic, T. Rajh, Nanostructured Layered Cathode for Rechargeable Mg-Ion Batteries, *ACS Nano.* 9 (2015) 8194–8205. <https://doi.org/10.1021/acsnano.5b02450>.
- [12] Z.-L. Tao, L.-N. Xu, X.-L. Gou, J. Chen, H.-T. Yuan, TiS_2 nanotubes as the cathode materials of Mg-ion batteries, *Chem. Commun.* (2004) 2080. <https://doi.org/10.1039/b403855j>.
- [13] Y. Liang, R. Feng, S. Yang, H. Ma, J. Liang, J. Chen, Rechargeable Mg Batteries with Graphene-like MoS_2 Cathode and Ultrasmall Mg Nanoparticle Anode, *Adv. Mater.* 23 (2011) 640–643. <https://doi.org/10.1002/adma.201003560>.
- [14] B. Liu, T. Luo, G. Mu, X. Wang, D. Chen, G. Shen, Rechargeable Mg-Ion Batteries Based on WSe_2 Nanowire Cathodes, *ACS Nano.* 7 (2013) 8051–8058. <https://doi.org/10.1021/nm4032454>.
- [15] Y. Tashiro, K. Taniguchi, H. Miyasaka, Copper Selenide as a New Cathode Material based on Displacement Reaction for Rechargeable Magnesium Batteries, *Electrochim. Acta.* 210 (2016) 655–661. <https://doi.org/10.1016/j.electacta.2016.05.202>.
- [16] F. Xiong, Y. Fan, S. Tan, L. Zhou, Y. Xu, C. Pei, Q. An, L. Mai, Magnesium storage performance and mechanism of CuS cathode, *Nano Energy.* 47 (2018) 210–216. <https://doi.org/10.1016/j.nanoen.2018.02.060>.

- [17] Y. NuLi, Y. Zheng, F. Wang, J. Yang, A.I. Minett, J. Wang, J. Chen, MWNT/C/Mg_{1.03}Mn_{0.97}SiO₄ hierarchical nanostructure for superior reversible magnesium ion storage, *Electrochem. Commun.* 13 (2011) 1143–1146. <https://doi.org/10.1016/j.elecom.2011.07.020>.
- [18] Y. Orikasa, T. Masese, Y. Koyama, T. Mori, M. Hattori, K. Yamamoto, T. Okado, Z.-D. Huang, T. Minato, C. Tassel, J. Kim, Y. Kobayashi, T. Abe, H. Kageyama, Y. Uchimoto, High energy density rechargeable magnesium battery using earth-abundant and non-toxic elements, *Sci. Rep.* 4 (2015) 5622. <https://doi.org/10.1038/srep05622>.
- [19] Y. Zheng, Y. NuLi, Q. Chen, Y. Wang, J. Yang, J. Wang, Magnesium cobalt silicate materials for reversible magnesium ion storage, *Electrochim. Acta.* 66 (2012) 75–81. <https://doi.org/10.1016/j.electacta.2012.01.037>.
- [20] J. Cabana, L. Monconduit, D. Larcher, M.R. Palacín, Beyond Intercalation-Based Li-Ion Batteries: The State of the Art and Challenges of Electrode Materials Reacting Through Conversion Reactions, *Adv. Mater.* 22 (2010) E170–E192. <https://doi.org/10.1002/adma.201000717>.
- [21] M. Wu, Y. Zhang, T. Li, Z. Chen, S. Cao, F. Xu, Copper sulfide nanoparticles as high-performance cathode materials for magnesium secondary batteries, *Nanoscale.* 10 (2018) 12526–12534. <https://doi.org/10.1039/C8NR03375G>.
- [22] Z. Wang, S. Rafai, C. Qiao, J. Jia, Y. Zhu, X. Ma, C. Cao, Microwave-Assisted Synthesis of CuS Hierarchical Nanosheets as the Cathode Material for High-Capacity Rechargeable Magnesium Batteries, *ACS Appl. Mater. Interfaces.* 11 (2019) 7046–7054. <https://doi.org/10.1021/acsami.8b20533>.
- [23] Y. Zhang, Y. Li, Y. Wang, R. Guo, W. Liu, H. Pei, G. Yin, D. Ye, S. Yu, J. Xie, A flexible copper sulfide @ multi-walled carbon nanotubes cathode for advanced

- magnesium-lithium-ion batteries, *J. Colloid Interface Sci.* 553 (2019) 239–246. <https://doi.org/10.1016/j.jcis.2019.06.027>.
- [24] J. Zhu, Q. Wu, J. Key, M. Wu, P.K. Shen, Self-assembled superstructure of carbon-wrapped, single-crystalline Cu_3P porous nanosheets: One-step synthesis and enhanced Li-ion battery anode performance, *Energy Storage Mater.* 15 (2018) 75–81. <https://doi.org/10.1016/j.ensm.2018.03.014>.
- [25] M.C. Stan, R. Klöpsch, A. Bhaskar, J. Li, S. Passerini, M. Winter, Cu_3P Binary Phosphide: Synthesis via a Wet Mechanochemical Method and Electrochemical Behavior as Negative Electrode Material for Lithium-Ion Batteries, *Adv. Energy Mater.* 3 (2013) 231–238. <https://doi.org/10.1002/aenm.201200655>.
- [26] G. Li, J. Tu, M. Wang, S. Jiao, Cu_3P as a novel cathode material for rechargeable aluminum-ion batteries, *J. Mater. Chem. A* 7 (2019) 8368–8375. <https://doi.org/10.1039/C9TA00762H>.
- [27] Q. Liang, Y. Zheng, C. Du, Y. Luo, J. Zhang, B. Li, Y. Zong, Q. Yan, General and Scalable Solid-State Synthesis of 2D MPS_3 ($\text{M} = \text{Fe}, \text{Co}, \text{Ni}$) Nanosheets and Tuning Their Li/Na Storage Properties, *Small Methods* 1 (2017) 1700304. <https://doi.org/10.1002/smtd.201700304>.
- [28] E. Edison, A. Chaturvedi, H. Ren, S. Sreejith, C.T. Lim, S. Madhavi, Route of Irreversible Transformation in Layered Tin Thiophosphate and Enhanced Lithium Storage Performance, *ACS Appl. Energy Mater.* (2018) acsaem.8b01357. <https://doi.org/10.1021/acsaem.8b01357>.
- [29] S. Huang, C. Meng, M. Xiao, S. Ren, S. Wang, D. Han, Y. Li, Y. Meng, Pseudocapacitive Sodium Storage by Ferroelectric $\text{Sn}_2\text{P}_2\text{S}_6$ with Layered Nanostructure, *Small* 14 (2018) 1704367. <https://doi.org/10.1002/smll.201704367>.

- [30] M. Wang, J. Han, W. Liu, M. Kamiko, S. Yagi, Energy storage mechanism of monocrystalline layered FePS_3 and FePSe_3 as active materials for Mg batteries and pseudocapacitors, *J. Alloys Compd.* 883 (2021) 160822. <https://doi.org/10.1016/j.jallcom.2021.160822>.
- [31] D. Tripathy, S. Sampath, Understanding the high capacity contributions of Cu_3PS_4 towards lithium storage, *J. Power Sources.* 478 (2020) 229066. <https://doi.org/10.1016/j.jpowsour.2020.229066>.
- [32] W. Brehm, A.L. Santhosha, Z. Zhang, C. Neumann, A. Turchanin, A. Martin, N. Pinna, M. Seyring, M. Rettenmayr, J.R. Buchheim, P. Adelhelm, Copper Thiophosphate (Cu_3PS_4) as Electrode for Sodium-Ion Batteries with Ether Electrolyte, *Adv. Funct. Mater.* 30 (2020) 1910583. <https://doi.org/10.1002/adfm.201910583>.
- [33] U. Pätzmann; W. Brockner, Vibrational Spectra of Ag_3PS_4 and Cu_3PS_4 , *Z. Naturforsch.* 38a (1983) 27–30. <https://doi.org/10.1515/zna-1983-0106>.
- [34] O. Sala, M.L.A. Temperini, Resonance raman effect of solid copper thiophosphate, *Chem. Phys. Lett.* 36 (1975) 652–654. [https://doi.org/10.1016/0009-2614\(75\)85359-0](https://doi.org/10.1016/0009-2614(75)85359-0).
- [35] S. Iqbal, H. Khatoon, A. Hussain Pandit, S. Ahmad, Recent development of carbon based materials for energy storage devices, *Mater. Sci. Energy Technol.* 2 (2019) 417–428. <https://doi.org/10.1016/j.mset.2019.04.006>.
- [36] Y. Zhang, D. Chen, X. Li, J. Shen, Z. Chen, S. Cao, T. Li, F. Xu, a $-\text{MoS}_3$ @CNT nanowire cathode for rechargeable Mg batteries: a pseudocapacitive approach for efficient Mg-storage, *Nanoscale.* 11 (2019) 16043–16051. <https://doi.org/10.1039/C9NR04280F>.
- [37] B.P. Vinayan, H. Euchner, Z. Zhao-Karger, M.A. Cambaz, Z. Li, T. Diemant, R.J. Behm, A. Gross, M. Fichtner, Insights into the electrochemical processes of

- rechargeable magnesium–sulfur batteries with a new cathode design, *J. Mater. Chem. A*. 7 (2019) 25490–25502. <https://doi.org/10.1039/C9TA09155F>.
- [38] P. Saha, P.H. Jampani, M.K. Datta, C.U. Okoli, A. Manivannan, P.N. Kumta, A Convenient Approach to Mo_6S_8 Chevrel Phase Cathode for Rechargeable Magnesium Battery, *J. Electrochem. Soc.* 161 (2014) A593–A598. <https://doi.org/10.1149/2.061404jes>.
- [39] W. Weppner, R.A. Huggins, Determination of the Kinetic Parameters of Mixed-Conducting Electrodes and Application to the System Li_3Sb , *J. Electrochem. Soc.* 124 (1977) 1569–1578. <https://doi.org/10.1149/1.2133112>.
- [40] M. Pelavin, D.N. Hendrickson, J.M. Hollander, W.L. Jolly, Phosphorus 2p electron binding energies. Correlation with extended Hueckel charges, *J. Phys. Chem.* 74 (1970) 1116–1121. <https://doi.org/10.1021/j100700a027>.
- [41] G.M. Currò, V. Grasso, F. Neri, L. Silipigni, The effects of the lithium intercalation on the X-ray photoelectron spectra of NiPS_3 , *Nuovo Cim. D.* 17 (1995) 37–52. <https://doi.org/10.1007/BF02451601>.

CRediT author statement

Debashis Tripathy: Data curation, Visualization; Formal analysis; Writing- Original draft preparation.

S Sampath: Conceptualization, Methodology; Writing review and editing; supervision

Journal Pre-proof

Declaration of interests

☒ The authors declare that they have no known competing financial interests or personal relationships that could have appeared to influence the work reported in this paper.

☐ The authors declare the following financial interests/personal relationships which may be considered as potential competing interests: